

**A Comparison of the Intrinsic Shapes of  
Two Different Types of Dwarf Galaxies:  
Blue Compact Dwarfs and Dwarf Ellipticals**

Eon-Chang Sung

Korea Astronomy Observatory, Taejon, Korea 305-348  
ecsung@hanul.issa.re.kr,

Cheongho Han

Department of Astronomy & Space Science,  
Chungbuk National University, Cheongju, Korea 361-763  
cheongho@astro-3.chungbuk.ac.kr,

Barbara S. Ryden

Department of Astronomy, The Ohio State University  
174 West 18th Avenue, Columbus, OH 43210  
ryden@astronomy.ohio-state.edu,

Mun-Suk Chun

Department of Astronomy,  
Yonsei University, Seoul, Korea 120-749  
mschun@galaxy.yonsei.ac.kr,

Ho-II Kim

Korea Astronomy Observatory, Taejon, Korea 305-348  
hikim@hanul.issa.re.kr.

Received \_\_\_\_\_; accepted \_\_\_\_\_

## ABSTRACT

We measure the apparent shapes for a sample of 62 blue compact dwarf galaxies (BCDs), and compare them with the apparent shapes for a sample of 80 dwarf elliptical galaxies (dEs). The BCDs are flatter, on average, than the dEs, but the difference is only marginally significant. We then use both non-parametric and parametric techniques to determine possible distributions of intrinsic shapes for the BCDs. The hypothesis that BCDs are oblate spheroids can be ruled out with a high confidence level ( $> 99\%$ ), but the hypothesis that they are prolate spheroids cannot be excluded. The apparent shapes of BCDs are totally consistent with the hypothesis that they are triaxial ellipsoids. If the intrinsic axis ratios,  $\beta$  and  $\gamma$ , are distributed according to a Gaussian with means  $\beta_0$  and  $\gamma_0$  and standard deviation  $\sigma$ , we find the best-fitting distribution for BCDs has  $(\beta_0, \gamma_0, \sigma) = (0.66, 0.55, 0.16)$ , while that for dEs has  $(\beta_0, \gamma_0, \sigma) = (0.85, 0.64, 0.24)$ . Our results are consistent with the hypothesis that BCDs have a close evolutionary relation with dEs.

*Subject headings:* galaxies: blue compact dwarf – galaxies: dwarf elliptical – galaxies: structure

submitted to *The Astrophysical Journal*: September 18, 1997  
Preprint: CNU-A&SS-04/97

## 1. Introduction

Understanding the formation and evolution of stellar systems like galaxies begins from the comparison of various observables. Dwarf galaxies are the most numerous type of galaxy in the universe. Nearly 80% of the known Local Group galaxies are dwarfs, and the number density of dwarf galaxies might be several dozen times that of giant spirals and ellipticals (Staveley-Smith, Davies, & Kinman 1992). The most common type of dwarf galaxy is the dwarf elliptical (hereafter dE). They have very smooth surface brightness profiles, which are typically nearly exponential (Sandage & Binggeli 1984; Caldwell & Bothun 1987). The dEs, like giant ellipticals, are found predominantly in groups and clusters of galaxies. Most dEs are symmetric and apparently relaxed with very uniform colors indicating that they are dominated by old stars (James 1994). The best-studied dwarf ellipticals are those in the Virgo cluster, cataloged by Sandage & Binggeli (1984) and Binggeli, Sandage, & Tammann (1985).

A smaller group of dwarf galaxies are classified as “blue compact dwarfs” (hereafter BCDs). In contrast to dEs, BCDs are undergoing intense bursts of star formation which give birth to a large number of massive stars, as evidenced by their blue  $UBV$  colors. These very young hot stars ionize the interstellar medium, producing high-excitation super-giant HII regions (Thuan 1991; Thuan, Izotov, & Lipovetsky 1995). As a result, the optical spectra of BCDs show strong narrow emission lines. Their ultraviolet spectra show a steeply rising continuum toward the blue, which is characteristic of OB stars (du Puy 1970; Searle & Sargent 1972).

In addition to these spectroscopic and spectrophotometric observations, another important tool for the comparison of different populations of dwarf galaxies is provided by morphological studies – for instance, the study of intrinsic shapes based on measured ellipticity distributions. There have been several trials which have explored this point: Caldwell (1983), Ichikawa, Wakamatsu, & Okamura (1986), Ichikawa (1989), Ferguson & Sandage (1989), and Ryden & Terndrup (1994) for dEs and Staveley-Smith et al. (1992) for BCDs. However, due to different observational techniques, different methods of measuring ellipticities, and different algorithms for deriving intrinsic shapes, direct comparison of the results might cause systematic errors. In addition, some previous studies suffered from additional systematic errors in eye-estimated flattening data (Fasano & Vio 1991; Ferguson & Binggeli 1994). Among the above authors, only the analysis of Ryden & Terndrup (1994) was based on CCD observations of a large data set. The analysis of Staveley-Smith et al. (1992) was also based on CCD observations; however, they determined the intrinsic shapes of BCDs under the (probably erroneous) assumption that all BCDs are oblate spheroids. In addition, the total size of their sample is too small to draw any strong conclusion. For studies of intrinsic shapes, a large homogeneous data set is essential.

In this paper, we measure the ellipticities of 62 BCDs, and compare the ellipticity distribution with that of a sample of 80 dEs (Ryden & Terndrup 1994; Ryden et al. 1997). The ellipticity distribution of BCDs proves to be marginally different from that of dEs. We then determine the distribution of intrinsic shapes for the BCDs, under various assumptions.

First, we assume that BCDs are either all oblate or all prolate, and use non-parametric analysis to find the best-fitting distribution of intrinsic shapes. Next, we assume that BCDs are triaxial, and use parametric analysis to find permissible distributions of intrinsic shapes. From these analyses, we find that the shapes of BCDs are well described either by triaxial ellipsoids or prolate spheroids; the hypothesis that BCDs are all oblate is ruled out. Similar results are obtained for dEs. If the intrinsic axis ratios,  $\beta$  and  $\gamma$ , are distributed according to a Gaussian with means  $\beta_0$  and  $\gamma_0$  and a common standard deviation of  $\sigma$ , we find the best-fitting intrinsic axis ratio distribution of BCDs has  $(\beta_0, \gamma_0, \sigma) = (0.66, 0.55, 0.16)$  with the KS probability of  $P_{\text{KS}} = 0.99$ , while that of dEs has  $(\beta_0, \gamma_0, \sigma) = (0.85, 0.64, 0.24)$  with  $P_{\text{KS}} = 0.97$ . Given the similarity of shape distributions, our results are consistent with the hypothesis that BCDs have a close evolutionary relation with dEs.

## 2. Observations

To measure the apparent axis ratios, we obtained images of 62 BCDs with the 1 m telescope at Mount Stromlo & Siding Spring Observatory. Eight observing sessions were carried out from 1993 April to 1994 March, employing a  $1024 \times 1024$  Tektronics chip, which provides a field of view of  $10' \times 10'$  with a pixel size of  $0''.57 \text{ pixel}^{-1}$ . The exposure time varied from 300 s to 600 s depending on the brightnesses of individual galaxies. We attempted to obtain the 4 (Bessell 1990) *BVRI* band images of individual BCDs. However, due to limited observing time, we obtained full 4-band images for only 35 out of 62 galaxies. For the other galaxies we obtained partial band images: 3 bands for 7 galaxies, 2 bands for another 7 galaxies, and only a single band image for the remaining 13 galaxies. Therefore, the total number of images is 188. The observed bands of each image are listed in Table 1.

We selected our sample of BCDs from various sources. We choose nearly half of our sample galaxies from the list of Thuan & Martin (1981); and the rest are from Maza et al. (1991), Bergvall & Olofsson (1986), Kunth & Sargent (1986), Macalpine & Williams (1981), Fairall (1977), Terlevich et al. (1991), Gondhaeker et al. (1984), Wamsteker et al. (1985), and Acker, Stenholm, & Verson (1991). The galaxies in these sources are classified as BCDs according to 3 major criteria:

1. low luminosity, with  $M_B \gtrsim -18$ ,
2. strong, sharp, narrow emission lines superimposed on a blue continuum,
3. very compact, with diameters of a few kpc.

To meet the necessities of observation and data analysis, we impose several additional criteria:

4. relatively small recession velocities ( $v \lesssim 4,000 \text{ km s}^{-1}$ ),
5. relatively bright apparent magnitudes ( $B < 16$ ),
6. relatively large angular sizes ( $\gtrsim 20''$ ),
7. unperturbed outer isophotes.

We include conditions 4 and 5 to select galaxies bright enough to obtain high  $S/N$  images

with the available telescope. Condition 6 is included because it is difficult to measure ellipticities precisely for galaxies of small angular size. According to the classification scheme of Loose & Thuan (1986), BCDs are classified into four types based on the regularity of the isophotal shapes of both the high surface brightness inner region, where star formation has recently occurred, and the low surface brightness outer region, which contains only an older stellar population. The first and most common type, comprising  $\sim 70\%$  of BCDs, is ‘iE’, which combines irregular inner isophotes with accurately elliptical outer isophotes. The ‘nE’ type has elliptical isophotes in both the inner and outer regions. The ‘iI’ type has irregular inner isophotes and outer isophotes that deviate measurably from perfect ellipses. Finally, ‘iO’ galaxies do not show faint outer structures at all; they appear to contain only starburst regions, and lack an underlying old stellar population. In our sample, we include all BCDs as long as their outer isophotes can be approximated as ellipses; our sample thus contains only iE, nE, and iI galaxies. However, we note that our sample represents the whole BCD population well because BCDs of type iO are very rare.

All steps of the data reduction and analysis were performed using a standard CCD reduction process with the Image Reduction and Analysis Facilities (IRAF). Raw images were first corrected for zero level bias and overscan pattern. Each image was then divided by a flat field obtained from the median of 5 – 10 twilight and dome flat images. During this process, pixels in the flat field image which are more than 1.5 times the median or less than 0.5 times the median are replaced with the median value. In addition, we combined images of individual galaxies if multiple images taken at the same bands are available. By combining images, we could not only correct for cosmic rays, but also increase signal-to-noise ratios. In the next stage, the sky brightness was subtracted from individual images. For sky subtraction of most BCD images, we used separate sky images taken just after the observation of each galaxy. However, if no sky image is available, we used the sky value in the vicinity of a galaxy within the same image. Finally, the processed images are trimmed centered at the galaxies. Since most BCDs in our sample have angular sizes less than  $2'$ , the typical trimmed images have sizes of  $\lesssim 500 \times 500$  pixel<sup>2</sup>. If stars are located on or near the galaxies, we remove them by replacing them with the median value of the area near the stars.

### 3. Determination of Apparent Axis Ratios

To determine intrinsic axis ratio distribution, one should start by measuring the apparent axis ratio,  $q = 1 - \epsilon = b/a$ , of galaxies, as projected onto the sky. Here  $a$  and  $b$  are the semimajor and semiminor axes of a projected galaxy, and  $\epsilon$  is the ellipticity. From the obtained image of each BCD, we measure the ellipticities as a function of semimajor axis from the center, using the Space Telescope Science Data Analysis System (STSDAS) routine ‘isophote’. In the routine, each galaxy was modeled as a nested series of ellipses, yielding the semimajor axis,  $a$ , position angle,  $\theta_{\text{pos}}$ , surface brightness,  $\Sigma(a)$ , and the positions of each ellipse’s center.

The ellipticities of the isophotes of many stellar systems vary as a function of semimajor axis. For BCDs we have the same problem of varying ellipticities, especially in the inner regions of BCDs. The main reason that makes the isophotes of a BCD deviate from well-aligned concentric ellipses is the existence of inner substructures, mainly bright HII regions (Thuan & Martin 1981; Gordon & Gottesman 1981). In Figure 1 we present, as an example, the  $B$ -band isophotes of ESO 495-G21, upon which are superimposed the best-fitting ellipses. To better show the poor ellipse fitting in the inner region of the galaxy, we expand the part enclosed by a box and present it in the upper right panel, in which the isophotes and corresponding best-fitting ellipses at  $a = 14.5$  and  $16.5$  are shown. We also present the ellipticity as a function of the semimajor axis in the lower panel. (Note that all length scales are in units of the pixel width.) The isophotes are distorted by a bright HII region located to the right of the galaxy’s center. As a result, the obtained best-fitting ellipses are more elongated than those which would be obtained without the HII region, and the position angle is tilted toward the direction of the HII region. Beyond a certain point ( $a \sim 30$  pixel for ESO 495-G21) there no longer exists any substructure, and the values of the ellipticity become stable as shown in the figure. Note that the concentric circles centered at  $(x, y) \sim (265, 220)$  and  $(x, y) \sim (262, 189)$  are foreground stars, before they are removed for ellipse fitting. The ellipse-fitting process fails as the surface brightness of a galaxy approaches background value; for the case of ESO 495-G21 this point corresponds to  $a \sim 95$ . Therefore, as a representative axis ratio of each BCD we determine the intensity-weighted axis ratio averaged over the intermediate region where stable ellipticities can be obtained with successful ellipse-fitting processes. The intensity-weighted mean axis ratio is computed by

$$\bar{q} = \frac{\int q(a)dL}{\int dL}; \quad dL = 2\pi qa \left[ 1 + \frac{1}{2} \frac{d \ln q(a)}{d \ln a} \right] \Sigma(a) da, \quad (1)$$

following the method by which Ryden & Terndrup (1994) computed the axis ratios of dEs. If more than a single band images are available, we take the mean value of the ellipticities determined in individual bands as a representative ellipticity. The finally determined ellipticities of our sample galaxies are listed in Table 1. We estimate the errors of  $\bar{\epsilon} = 1 - \bar{q}$  by computing the variance of  $\epsilon(a)$  within the range of semimajor axis where ellipticities are measured.

A BCD with lots of star formation might have a  $B$  image different from its  $I$  image, for instance; the  $B$  image emphasizes star formation regions, and hence is much clumpier. Thus, the measured ellipticities at  $B$  might be systematically different from the ellipticities in other bands. To test this possibility, in Figure 2 we compare the ellipticities measured in  $B$  band,  $\epsilon_B$ , to those measured in  $I$  band,  $\epsilon_I$ . Ellipticities do not vary significantly from one band to another. The values of ellipticities are consistent regardless of the observed bands because the determination of  $\bar{\epsilon}$  depends strongly on the ellipticities beyond the inner clumpy regions.

We also check the consistency of our measurements by measuring ellipticities in a different way. In the second method, we measure the ellipticity  $\epsilon_{24}$  at the point where the surface brightness is  $\Sigma_B = 24 \text{ mag arcsec}^{-2}$ . For these determinations, we carried

out  $B$ -band surface photometry of arbitrarily selected 16 sample BCDs by using elliptical isophote fitting method with the STSDAS routine ‘isophote’. Photometric calibrations were carried out by using  $\sim 50$  standard stars in the list of Graham (1982) and Landolt (1992). In Figure 3, we plot the correlation between  $\bar{\epsilon}$  and  $\epsilon_{24}$ . The ellipticities determined in both ways are consistent each other. In Figure 3, the error estimates of  $\epsilon_{24}$  are derived by computing the standard deviation of isophotes from their corresponding best-fitting ellipses, i.e.,  $\sigma_{\epsilon_{24}} = [\sum(\mathbf{x}_{\text{isophote}} - \mathbf{x}_{\text{ellipse}})^2/n_{\text{point}}]^{1/2}$ . Here  $\mathbf{x}_{\text{isophote}}$  and  $\mathbf{x}_{\text{ellipse}}$  represent the positions of isophotes and ellipses on CCD pixel coordinates, and  $n_{\text{point}}$  is the number of pixels on which individual curves (both isophotes and ellipses) are drawn.

Since we use the same method for determining  $\bar{\epsilon}$  as Ryden & Terndrup (1994), we can directly compare our results for the apparent shapes of BCDs to their results for the apparent shapes of dEs in the Virgo Cluster. To the data obtained for 70 dEs by Ryden & Terndrup (1994), we add data for an additional 10 dEs observed in Virgo by Ryden et al. (1997). The cumulative distribution function of  $\bar{q} = 1 - \bar{\epsilon}$  for the 62 BCDs is shown as the solid step function in Figure 4. The cumulative distribution function of  $\bar{q}$  for the 80 Virgo dEs is shown as the dotted step function in the same Figure. A Kolmogorov-Smirnov test comparing the two distributions shows a marginal difference, with  $P_{\text{KS}} = 0.057$ . The main difference between the apparent axis ratios of the two distributions is that BCDs are slightly flatter, on average. For the sample of BCDs, the mean and standard deviation of  $\bar{q}$  are  $0.671 \pm 0.150$ ; for the sample of dEs, they are  $0.719 \pm 0.156$ . A Mann-Whitney U-test comparing the medians of the two data sets yields a probability  $P_{\text{MW}} = 0.068$ . Thus, we can state from the Mann-Whitney test that the two distributions differ at the 93.2% confidence level.

#### 4. Intrinsic Shape Determination

The apparent axis ratio distributions of stellar systems provide important constraints about the 3-dimensional shapes of the systems (Fasano & Vio 1991; Lambas, Maddox, & Loveday 1992; Tremblay & Merritt 1995; Ryden 1992, 1996). For the determination of intrinsic shapes, two methods are often applied. Both methods assume that the galaxies which we observe are randomly oriented with respect to us. The first method for determining intrinsic shapes assumes that the galaxies are intrinsically axisymmetric, and that they are either all oblate or all prolate. With these assumptions, one can perform a unique mathematical inversion to go from the distribution  $f(q)$  of apparent shapes to the distribution  $f(\gamma)$  of intrinsic shapes. The second method assumes that galaxies are triaxial; in this case one no longer has a unique solution to the problem. However, if one assumes a functional form (e.g., Gaussian) for the distribution of intrinsic axis ratios, one can vary the parameters of the function until one finds the model which best fits the observed distribution of apparent axis ratios. Parametric fits are useful because they enable us to see how statistics such as the  $\chi^2$  and KS scores vary as the parameters are changed. We estimate the intrinsic shapes of BCDs by using both the non-parametric and the parametric

methods.

#### 4.1. Non-parametric Method

Using the non-parametric method, we reject or accept, at a known confidence level, the null hypothesis that the intrinsic shapes of the galaxies in a sample are randomly oriented oblate spheroids. Moreover, if the null hypothesis is not rejected, the non-parametric method gives an estimate for the distribution function  $f_o$  of the galaxies' intrinsic axis ratios,  $\gamma \leq 1$ . Similarly, we can reject or accept the hypothesis that they are randomly oriented prolate spheroids. To accomplish this, we make a non-parametric kernel estimate  $f(q)$  of the distribution of the apparent axis ratio  $q$ . We then mathematically invert  $f(q)$  to find  $f_o(\gamma)$  and  $f_p(\gamma)$ , the estimated distributions of the intrinsic axis ratio  $\gamma$  for a population of oblate and prolate spheroids, respectively. Confidence intervals are placed on the estimators  $f(q)$ ,  $f_o$ , and  $f_p$  by performing repeated bootstrap resampling of the observed data and creating new estimates from each sample. The spread in the bootstrap estimates of  $f$  at a given value of  $q$  and of  $f_o$  and  $f_p$  at a given value of  $\gamma$  provides confidence intervals for the non-parametric estimates of these functions. Once the estimators  $f_o$  and  $f_p$  are determined, one can exclude the oblate or prolate hypothesis at a given confidence level if the upper confidence limit drops below zero for any value of the intrinsic axis ratio  $\gamma$ . For the details of the non-parametric kernel estimators, see Ryden (1996) and Tremblay & Merritt (1995).

In the upper panel of Figure 5a, we present the non-parametric kernel estimate of the distribution of the apparent axis ratios for our sample of 62 BCDs. In the following panels, we also present the distributions of intrinsic axis ratios assuming that the BCDs are oblate (middle) and prolate (bottom). The solid line in each panel is the best estimate, the dashed lines are the 80% confidence band, and the dotted lines are the 98% confidence band. (That is, 10% of the bootstrap resamplings lie above the 80% confidence band, and 10% lie below it. Similarly, 1% of the resamplings lie above the 98% confidence band, and 1% lie below it.) The hypothesis that BCDs are randomly oriented oblate spheroids is ruled out at the 99% (one-sided) confidence level. Due to the lack of nearly circular BCDs (those with  $q \sim 1$ ), the 98% confidence band for  $f_o$  dips far below zero at  $\gamma > 0.9$ . On the other hand, the prolate hypothesis cannot be ruled out at the 99% (one-sided) confidence level. The best-fitting prolate distribution (the solid line in the bottom panel of Figure 5a) gives a mean and standard deviation for the intrinsic axis ratio  $\gamma$  of  $0.58 \pm 0.13$ .

For the comparison of intrinsic shape of BCDs with that of dEs we also present  $f(q)$ ,  $f_o$ , and  $f_p$  for the sample of 80 Virgo dEs, in Figure 5b. We find that the oblate hypothesis cannot be ruled out at the 99% (one-sided) confidence level for this sample, while the prolate hypothesis is *perfectly* acceptable. The best-fitting prolate distribution gives a mean and standard deviation for  $\gamma$  of  $0.63 \pm 0.15$ . Ryden (1996), analyzing a set of 170 Virgo dEs observed by Binggeli & Cameron (1993), found that for this larger sample, the oblate hypothesis can be ruled out at the 99% confidence level. By contrast, Ichikawa (1989), analyzing a sample of 98 Virgo dEs, alleges that their apparent shapes are consistent with



their being a population of oblate spheroids. Instead of doing a non-parametric analysis, Ichikawa used Gaussian approximations to the correct values of  $f_o$  and  $f_p$ , finding that a Gaussian with mean and standard deviation  $(\gamma_0, \sigma) \sim (0.6, 0.06)$  is the best fit for a population of oblate spheroids. However, although this is the best fit, it is not a good fit. Although he does not provide a  $\chi^2$  probability, fig 1(a) of his paper shows very poor fit; the best-fitting distribution overestimates the number of nearly circular dEs and severely underestimates the number of apparently highly flattened dEs. Thus, Ichikawa’s results, like ours, indicate that the oblate hypothesis yields a poor fit to the observed distribution of apparent axis ratios. Ichikawa also presented the best-fitting distribution under prolate hypothesis with  $(\gamma_0, \sigma) \sim (0.64, 0.12)$ , which is very similar to our determination of the mean and standard deviation of  $\gamma$  for prolate dEs.

## 4.2. Parametric Method

For the parametric determination of the intrinsic axis ratio distribution of BCDs, we follow the assumptions of Ryden & Terndrup (1994); that galaxies are triaxial ellipsoids with axis ratios  $1 \geq \beta \geq \gamma$ , and that the distribution of intrinsic axis ratios follows a Gaussian distribution with means  $\beta_0$  and  $\gamma_0$  and a common width  $\sigma$ ; i.e.,

$$f(\beta, \gamma) \propto \exp \left[ -\frac{(\beta - \beta_0)^2 + (\gamma - \gamma_0)^2}{2\sigma^2} \right]. \quad (2)$$

With these assumptions we produce a large number ( $10^4$ ) of test BCDs whose intrinsic axis ratios are distributed according to equation (2). Then we compute their projected axis ratios assuming that BCDs are randomly oriented with respect to us. When an triaxial ellipsoid is projected with the viewing angles of  $\theta$  and  $\phi$ , it appears as an ellipse with an apparent axis ratio of

$$q(\beta, \gamma, \theta, \phi) = \left[ \frac{A + C - \sqrt{(A - C)^2 + B^2}}{A + C + \sqrt{(A - C)^2 + B^2}} \right]^{1/2}, \quad (3)$$

where

$$\begin{cases} A = (\cos^2 \phi + \beta^2 \sin^2 \phi) \cos^2 \theta + \gamma^2 \sin^2 \theta, \\ B = \cos \theta \sin 2\phi (1 - \beta^2), \\ C = \sin^2 \phi + \beta^2 \cos^2 \phi \end{cases} \quad (4)$$

(Binney 1985). The cumulative distribution of the projected axis ratios of the test BCDs is then compared with the observed one by using Kolmogorov-Smirnov (KS) tests; we additionally apply  $\chi^2$  tests to the binned distributions.

Figure 6a and 6b show the isoprobability contours on 4 slices through the  $(\beta_0, \gamma_0, \sigma)$  parameter space, as measured by KS and  $\chi^2$  tests, respectively. When measured by KS tests the best-fitting distribution has parameters of  $(\beta_0, \gamma_0, \sigma) = (0.66, 0.55, 0.16)$  with the

KS probability of  $P_{\text{KS}} = 0.99$ , implying that the intrinsic shape of BCDs can be well fitted by a population of triaxial ellipsoids. We obtain consistent results when measured by  $\chi^2$  tests; the best-fitting distribution has parameters of  $(\beta_0, \gamma_0, \sigma) = (0.77, 0.51, 0.16)$  with the  $\chi^2$  probability of  $P_{\chi^2} = 0.96$ .

For the 80 dE galaxies from Ryden & Terndrup (1994) and Ryden et al. (1997), the best-fitting parametric model, as measured by a KS test, had  $(\beta_0, \gamma_0, \sigma) = (0.85, 0.64, 0.24)$ , with  $P_{\text{KS}} = 0.97$ . In Figure 7, we show four slices through parameter space, showing the isoproability contours for the parametric dE models as measured by KS tests. When the best-fitting distributions for dEs are compared to that of BCDs, one finds that the dEs are rounder, but the difference is not greatly significant.

In Figure 4, we present the cumulative distributions of apparent axis ratios for BCDs (solid step function) and dEs (dotted step function). On top of each observed distribution we overlay the expected distribution from the best-fitting triaxial model, as measured by a KS test. For BCDs, the prediction of the best-fitting model, with  $(\beta_0, \gamma_0, \sigma) = (0.66, 0.55, 0.16)$ , is given by the solid smooth line. For dEs, the prediction of the best-fitting model, with  $(\beta_0, \gamma_0, \sigma) = (0.85, 0.64, 0.24)$ , is given by the dotted smooth line.

## 5. Discussion

The results of our morphological analysis based on 62 BCDs and 80 dEs are summarized as follows.

1. The apparent shapes of both BCDs and dEs can be explained by their being either triaxial ellipsoids or prolate spheroids.
2. However, it is unlikely that the intrinsic shapes of either BCDs and dEs are purely oblate spheroids.
3. Compared to dEs, BCDs are flatter, but the difference between the apparent axis ratio distributions of BCDs and dEs is marginal.

The nature of BCDs remains ambiguous and confusing (Papaderos et al. 1996), and thus theories to explain their nature are very controversial. There are two major competing hypotheses. The first one claims that BCDs are basically a different population from dEs. According to this scenario BCDs are truly young systems, in which the present starburst is the first in the galaxy’s lifetime. The other model suggests that BCDs might be dEs which are mainly composed of old stellar populations, and that the observed spectroscopic features and the spectral energy distributions are attributed to a recent burst of star formation. That is, BCDs are basically dEs seen during a brief episode ( $t \sim 10^7$  yr) of violent star formation.

Although strong conclusions cannot be derived just from a single comparison of morphology, the similarity between the intrinsic shapes of BCDs and dEs may give support to the second hypothesis that BCDs are just a sub-population of dEs that have undergone a recent burst of star formation. The second hypothesis is also supported by other

observations. Thuan (1983) argued that the near-infrared emission in the vast majority of BCDs is attributable to old K and M stars, which are the major components of dEs; Hunter & Gallagher (1985) also agreed that young stars are not the major contributors to the near-infrared flux of BCDs. In addition, many BCDs, like dEs, have surface brightness profiles that are well fitted by exponentials. For example, Haro 2 was classified as a BCD by Haro (1956) and Markarian (1967), based on its spectral features. By contrast, Loose & Thuan (1986) claimed that Haro 2 should be classified as a dE, based on its surface brightness profiles.

The question of how to explain the difference in spectra between the two types of dwarf galaxy still remains. Drinkwater & Hardy (1991) stated that BCDs, after the end of starburst activity, fade to form dEs, as the amount of gas decreases by stripping. On the other hand, Silk, Wyse, & Shields (1987) proposed a totally reversed evolution sequence: from dEs to BCDs. According to them, hot gas, left over from the galaxy formation era, is trapped in a galaxy group, cools and accretes onto dEs, and provokes an intense burst of star formation. As a result, dEs are transformed into BCDs. Although our results cannot clearly designate the direction of evolution, they suggest some evolutionary relation between the two systems.

We would like to thank staffs at the Mt. Stromlo & Siding Spring Observatory, especially K. C. Freeman for supporting observations. We also thank D. M. Terndrup, R. W. Pogge, and T. R. Lauer for kindly providing additional flattening data of dwarf ellipticals. E.-C. S. has been supported by Basic Research Fund of Korea Astronomy Observatory. B. S. R. was supported by grant NSF AST-93-577396.

## REFERENCES

- Acker, A., Stenholm, B., & Verson, P. 1991, *A&AS*, 87, 449
- Bergvall, N., & Olofsson, K. 1986, *A&AS*, 64, 469
- Bessell, M. S. 1990, *PASP*, 102, 1181
- Binggeli, B., Sandage, A., & Tammann, G. A. 1985, *AJ*, 90, 1681
- Binggeli, B., & Cameron, L. M. 1993, *A&AS*, 98, 297
- Binney, J. 1985, *MNRAS*, 212, 767
- Caldwell, N. 1983, *AJ*, 88, 804
- Caldwell, N., & Bothun, G. D. 1987, *AJ*, 94, 1126
- Drinkwater, M., & Hardy, E. 1991, *AJ*, 101, 94
- du Puy, D. L. 1970, *AJ*, 75, 1143
- Fairall, A. P. 1977, *MNRAS*, 180, 391
- Fasano, G., & Vio, R. 1991, *MNRAS*, 249, 629
- Ferguson, H. C., & Sandage, A. 1989, *ApJ*, 346, L53
- Ferguson, H. C., & Binggeli, B. 1994, *A&A Rev.*, 6, 67
- Gondhaeker, P. M., Morgas, D. H., Dopita, M., & Phillip, A. P. 1984, *MNRAS*, 209, 59
- Gordon, D., & Gottesman, S. T. 1981, *AJ*, 86, 161
- Graham, J. A. 1982, *PASP*, 94, 244
- Haro, G. 1956, *Bol. Obs. Tomantzintla y Tacubaya*, 14, 8
- Hunter, D. A., & Gallagher, J. S. 1985, *ApJS*, 58, 533
- Ichikawa, S.-I. 1989, *AJ*, 97, 1600
- Ichikawa, S.-I., Wakamatsu, K.-I., & Okamura, S. 1986, *ApJS*, 60, 475
- James, P. A. 1994, *MNRAS*, 269, 176
- Kunth, D., & Sargent, W. L. W. 1986, *AJ*, 91, 761
- Lambas, D. S., Maddox, S. J., & Loveday, J. 1992, *MNRAS*, 258, 404
- Landolt, A. U. 1992, *AJ*, 104, 340
- Loose, H. H., & Thuan, T. X. 1986, in *Star-Forming Dwarf Galaxies and Related Objects*, ed. D. Kunth, T. X. Thuan, & T. T. Van (Paris: Editions Frontières), 73
- Macalpine, G. M., & Williams, G. A. 1981, *ApJS*, 45, 113
- Markarian, B. E. 1967, *Astrofizika*, 3, 55
- Maza, J., Ruiz, M. T., Pena, M., Gonzalez, L. E., & Wischnjewsky, M. 1991, *A&AS*, 89, 389
- Papaderos, P., Loose, H.-M., Fricke, K. J., & Thuan, T. X. 1996, *A&A*, 314, 59

- Ryden, B. S. 1992, *ApJ*, 396, 445
- Ryden, B. S. 1996, *ApJ*, 461, 146
- Ryden, B. S., & Terndrup, D. M. 1994, *ApJ*, 425, 43
- Ryden, B. S., Terndrup, D. M., Pogge, R. W., & Lauer, T. R. 1997, *ApJ*, submitted
- Sandage, A., & Binggeli, B. 1984, *AJ*, 89, 919
- Searle, L., & Sargent, W. L. 1972, *ApJ*, 173, 25
- Silk, J., Wyse, R. F. G., & Shields, G. A. 1987, *ApJ*, 322, L59
- Staveley-Smith, L., Davies, R. D., & Kinman, T. D. 1992, *MNRAS*, 258, 334
- Terlevich, R., Melnick, J., Masegosa, J., Moles, M., & Copetti, M. V. F. 1991, *A&AS*, 91, 285
- Thuan, T. X. 1983, *ApJ*, 268, 667
- Thuan, T. 1991, in *Proceedings of the Massive Stars in Starbursts*, ed. C. Leitherer, N. R. Walborn, T. M. Heckman, & C. A. Norman (Cambridge: Cambridge University Press), 183
- Thuan, T. X., Izotov, Y. I., & Lipovetsky, V. A. 1995, *ApJ*, 445, 108
- Thuan, T. X., & Martin, G. E. 1981, *ApJ*, 247, 823
- Tremblay, B., & Merritt, D. 1995, *AJ*, 110, 1039
- Wamsteker, W., Prieto, A., Vitores, A., Schuster, H. E., Danks, A. C., Gonzalez, R., & Rodriguez, G. 1985, *A&AS*, 62, 255

TABLE 1  
THE INTENSITY WEIGHTED MEAN ELLIPTICITIES

name	band	$\bar{\epsilon} \pm \Delta\epsilon$	name	band	$\bar{\epsilon} \pm \Delta\epsilon$
CTS 1010	<i>V, R</i>	$0.387 \pm 0.064$	ESO 508-G33	<i>B</i>	$0.149 \pm 0.202$
CTS 1020	<i>B, I</i>	$0.244 \pm 0.021$	ESO 554-IG27	<i>B, V, R, I</i>	$0.323 \pm 0.057$
CTS 1025	<i>V</i>	$0.352 \pm 0.070$	Fairall 67	<i>B, V, R, I</i>	$0.371 \pm 0.010$
CTS 1033	<i>B</i>	$0.577 \pm 0.000$	Fairall 177	<i>B, V, R, I</i>	$0.234 \pm 0.038$
CTS 1034	<i>B</i>	$0.089 \pm 0.207$	Fairall 318	<i>B, V</i>	$0.405 \pm 0.025$
CTS 1037	<i>B, V, R</i>	$0.141 \pm 0.007$	Fairall 346	<i>B, V, R, I</i>	$0.188 \pm 0.011$
CTS 1040	<i>B, V, R</i>	$0.205 \pm 0.020$	G0003-41	<i>I</i>	$0.463 \pm 0.037$
CTS 1042	<i>B, V, R, I</i>	$0.357 \pm 0.010$	Haro 6	<i>B, V, R, I</i>	$0.136 \pm 0.021$
ESO 037-G03	<i>B, V, I</i>	$0.411 \pm 0.028$	Haro 14	<i>B, V, R, I</i>	$0.139 \pm 0.025$
ESO 092-G02	<i>V</i>	$0.331 \pm 0.056$	Haro 15	<i>B, V, R, I</i>	$0.259 \pm 0.035$
ESO 102-G14	<i>B</i>	$0.317 \pm 0.015$	Haro 18	<i>B, V, R, I</i>	$0.143 \pm 0.022$
ESO 105-IG11	<i>B, V, R, I</i>	$0.458 \pm 0.031$	Haro 20	<i>B, V, R, I</i>	$0.474 \pm 0.008$
ESO 148-IG07	<i>B, R</i>	$0.200 \pm 0.059$	Haro 21	<i>B, V, R, I</i>	$0.211 \pm 0.037$
ESO 156-G38	<i>B, V, R, I</i>	$0.327 \pm 0.025$	II Zw 40	<i>V</i>	$0.415 \pm 0.035$
ESO 185-IG13	<i>B, V, R, I</i>	$0.180 \pm 0.025$	Mrk 49	<i>B, V, R, I</i>	$0.226 \pm 0.012$
ESO 249-G13	<i>B, V</i>	$0.686 \pm 0.046$	Mrk 400	<i>B, V, R, I</i>	$0.481 \pm 0.021$
ESO 250-G03	<i>B, V, R, I</i>	$0.122 \pm 0.020$	Mrk 527	<i>B</i>	$0.364 \pm 0.019$
ESO 286-IG19	<i>B, V</i>	$0.389 \pm 0.046$	NGC 1705	<i>B, V, R, I</i>	$0.274 \pm 0.014$
ESO 338-IG04	<i>B, V</i>	$0.343 \pm 0.016$	NGC 5253	<i>B, V, R, I</i>	$0.527 \pm 0.010$
ESO 352-G67	<i>B, V, R, I</i>	$0.164 \pm 0.023$	Pox 36	<i>B, V, R, I</i>	$0.540 \pm 0.024$
ESO 379-G17	<i>B, V, I</i>	$0.080 \pm 0.121$	Pox 139	<i>I</i>	$0.510 \pm 0.080$
ESO 386-G19	<i>B, V, R, I</i>	$0.144 \pm 0.022$	T1258-363	<i>B</i>	$0.340 \pm 0.033$
ESO 422-G03	<i>B, V, R, I</i>	$0.458 \pm 0.006$	T1324-276	<i>B, V, R, I</i>	$0.569 \pm 0.011$
ESO 435-IG20	<i>B, V, R, I</i>	$0.412 \pm 0.019$	T2138-397	<i>B, V, R, I</i>	$0.341 \pm 0.039$
ESO 462-IG20	<i>B, V, R, I</i>	$0.158 \pm 0.030$	T2259-398	<i>B, V, I</i>	$0.041 \pm 0.010$
ESO 480-IG08	<i>B, V, R, I</i>	$0.296 \pm 0.009$	T2311-411	<i>B</i>	$0.313 \pm 0.033$
ESO 480-IG12	<i>B, V, I</i>	$0.545 \pm 0.017$	Tololo 3	<i>B, V, R, I</i>	$0.311 \pm 0.042$
ESO 483-G13	<i>B, V, R, I</i>	$0.394 \pm 0.009$	UM 40	<i>B, V, R, I</i>	$0.467 \pm 0.022$
ESO 495-G21	<i>B, V, R, I</i>	$0.158 \pm 0.013$	UM 69	<i>B, V, R, I</i>	$0.589 \pm 0.010$
ESO 502-IG11	<i>V</i>	$0.547 \pm 0.041$	UM 448	<i>B, V, R, I</i>	$0.311 \pm 0.016$
ESO 505-G12	<i>B, V, R, I</i>	$0.259 \pm 0.014$	UM 621	<i>B, V, R</i>	$0.520 \pm 0.017$

NOTE.— The intensity weighted mean ellipticities of 62 BCDs. Also listed are the observed bands for each image.

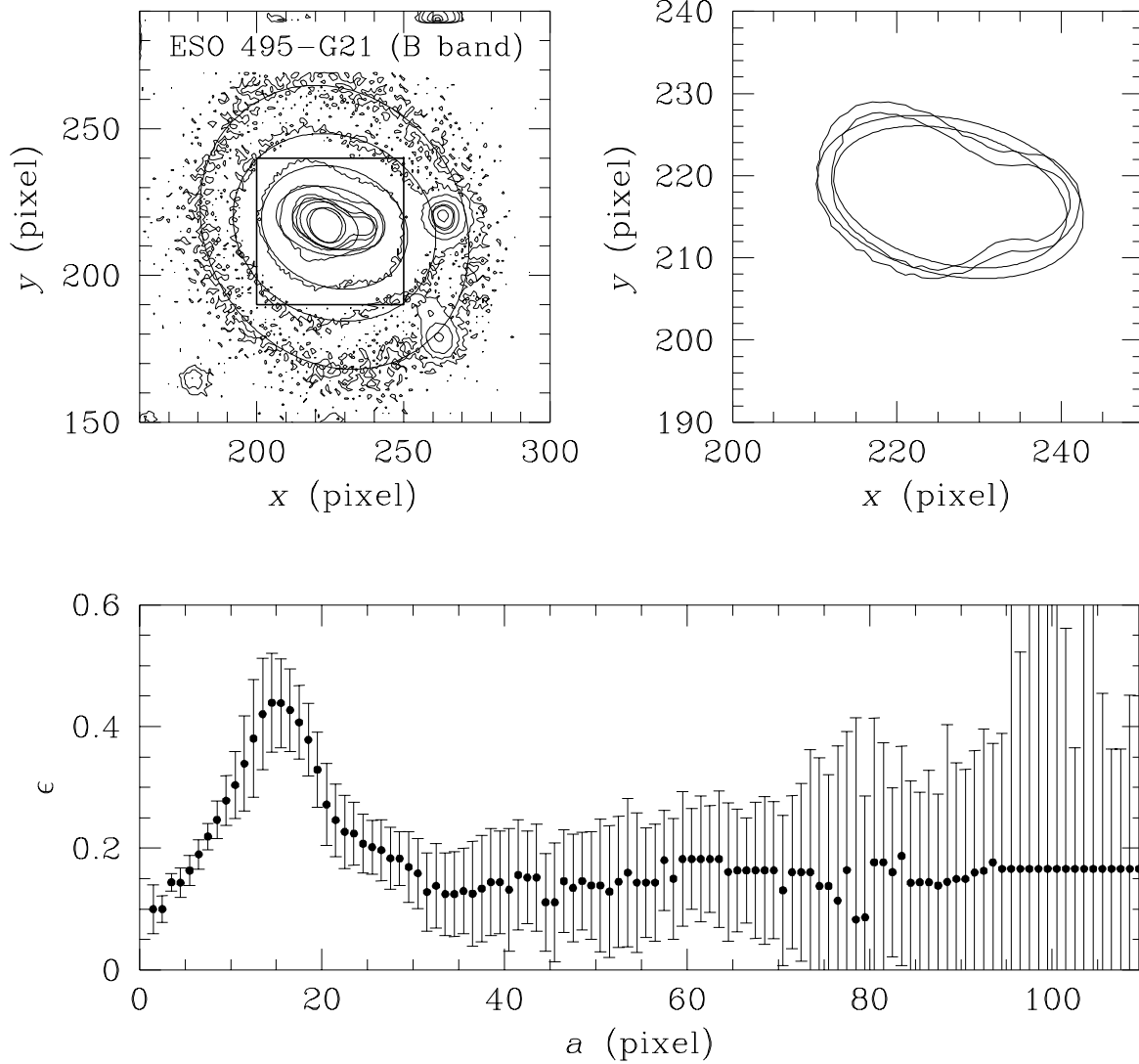


**Figure 1:** Upper panels: the  $B$ -band isophotes of ESO 495-G21, with the best-fitting ellipses superimposed. To better show the ellipse fits for the inner isophotes, the region enclosed by a box is expanded and shown in the upper right panel, where the best-fitting ellipses at  $a = 14.5$  and  $16.5$  and corresponding isophotes are presented. Note the length scales are given by pixel values, which correspond to  $0''.57/\text{pixel}^{-1}$ . Lower panel: the determined ellipticity of ESO 495-G21 as a function of semimajor axis. Error estimates for  $\epsilon(a)$  are derived by computing the standard deviation of isophotes from their best-fitting ellipses.

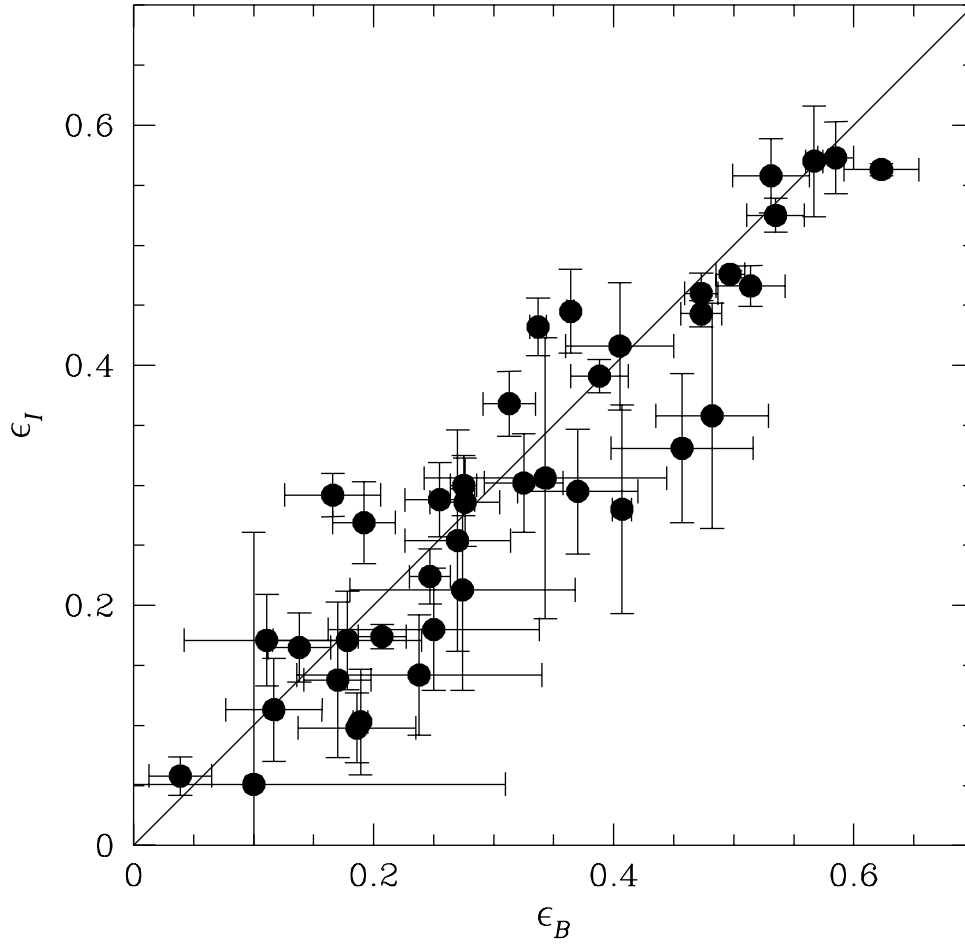


**Figure 2:** The correlation between ellipticities determined in  $B$  and  $I$  bands. The solid line across the panel represents the identity between the two measurements, and is not a fit to the data. The errors in each band are estimated by computing the standard deviations of isophotes from the best-fitting ellipses.



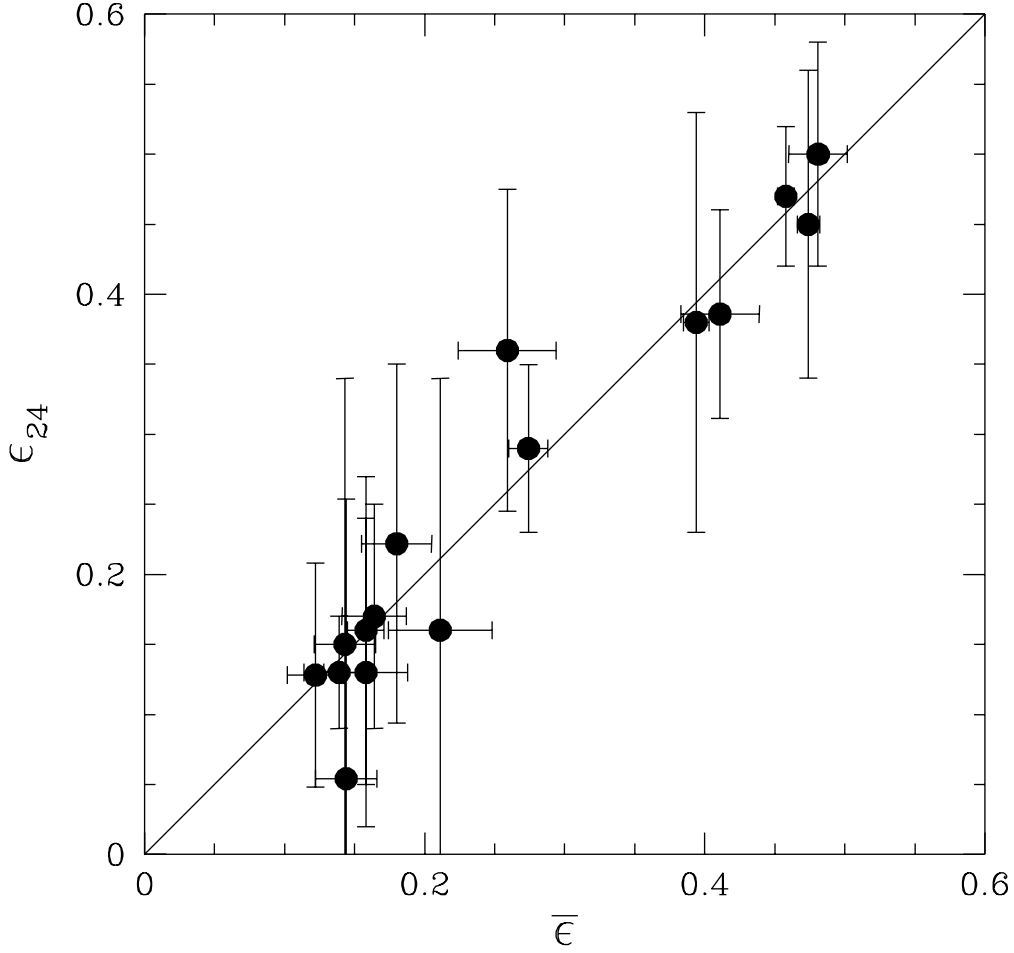


**Figure 3:** The correlation between the intensity-weighted ellipticity,  $\bar{\epsilon}$ , and the ellipticity of the  $\Sigma_B = 24$  mag isophote,  $\epsilon_{24}$ , for a randomly selected sample of 16 BCDs. The solid line across the panel represents the identity between the two measurements. The errors of  $\epsilon_{24}$  are estimated by computing the standard deviations of isophotes from the best-fitting ellipses, while those for  $\bar{\epsilon}$  are determined from the variance of  $\epsilon(a)$ .

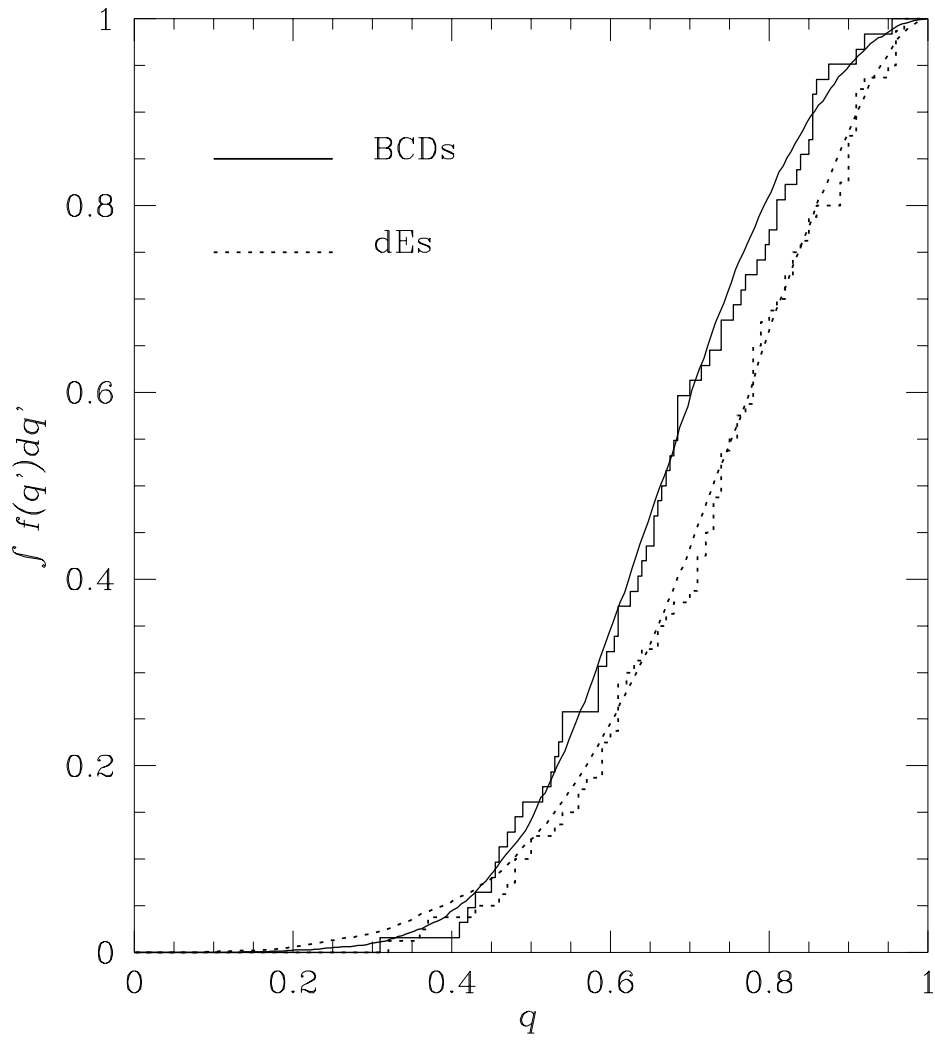


**Figure 4:** The cumulative distribution of apparent axis ratios for 62 BCDs (solid line) and 80 dEs (dotted line). The step function, in each case, is the data; the smooth curve superimposed is the predicted distribution of apparent shapes from the best-fitting triaxial model.

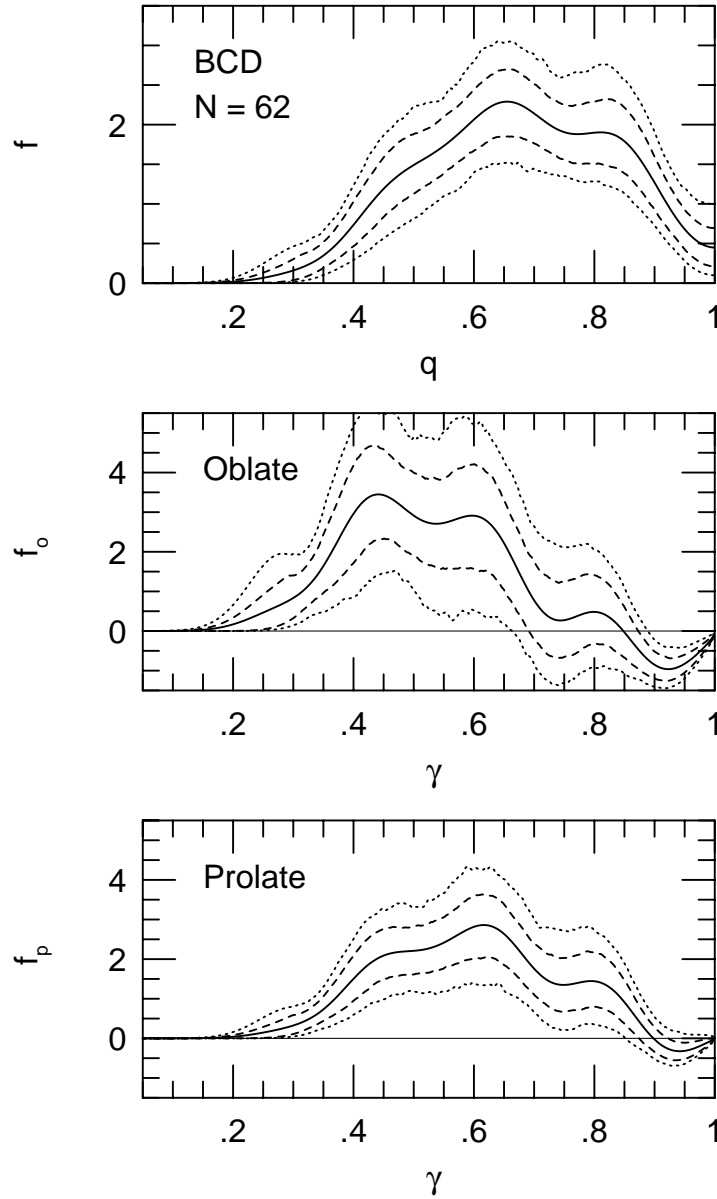


**Figure 5a:** The non-parametric kernel estimate of the distribution of a sample of 62 BCDs (top panel). Also shown are the distributions of intrinsic axis ratios, assuming BCDs are all oblate (middle panel) and all prolate (bottom panel). The solid line in each panel is the best estimate, the dashed lines are the 80% confidence band, and dotted lines are the 98% confidence band.

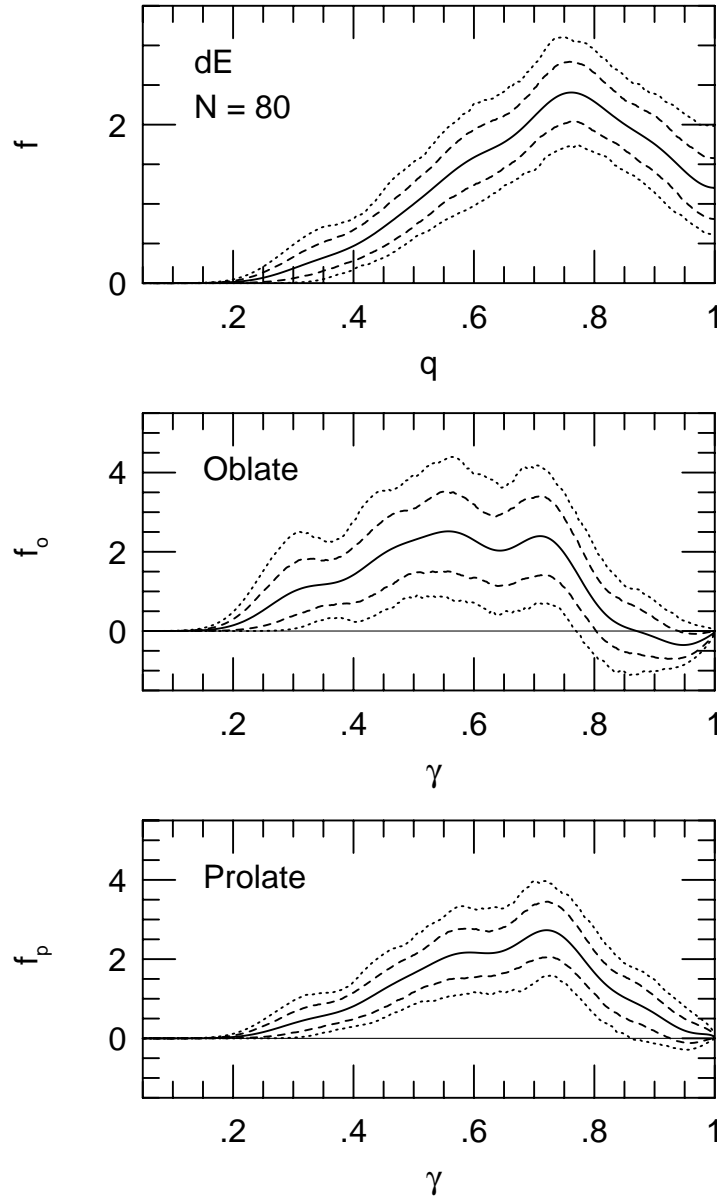


**Figure 5b:** The non-parametric kernel estimate of the distribution of a sample of 80 dEs (top panel). The distributions of intrinsic axis ratios under all oblate (middle panel) and all prolate (bottom panel) are also shown. The confidence bands are same as in Figure 5a.

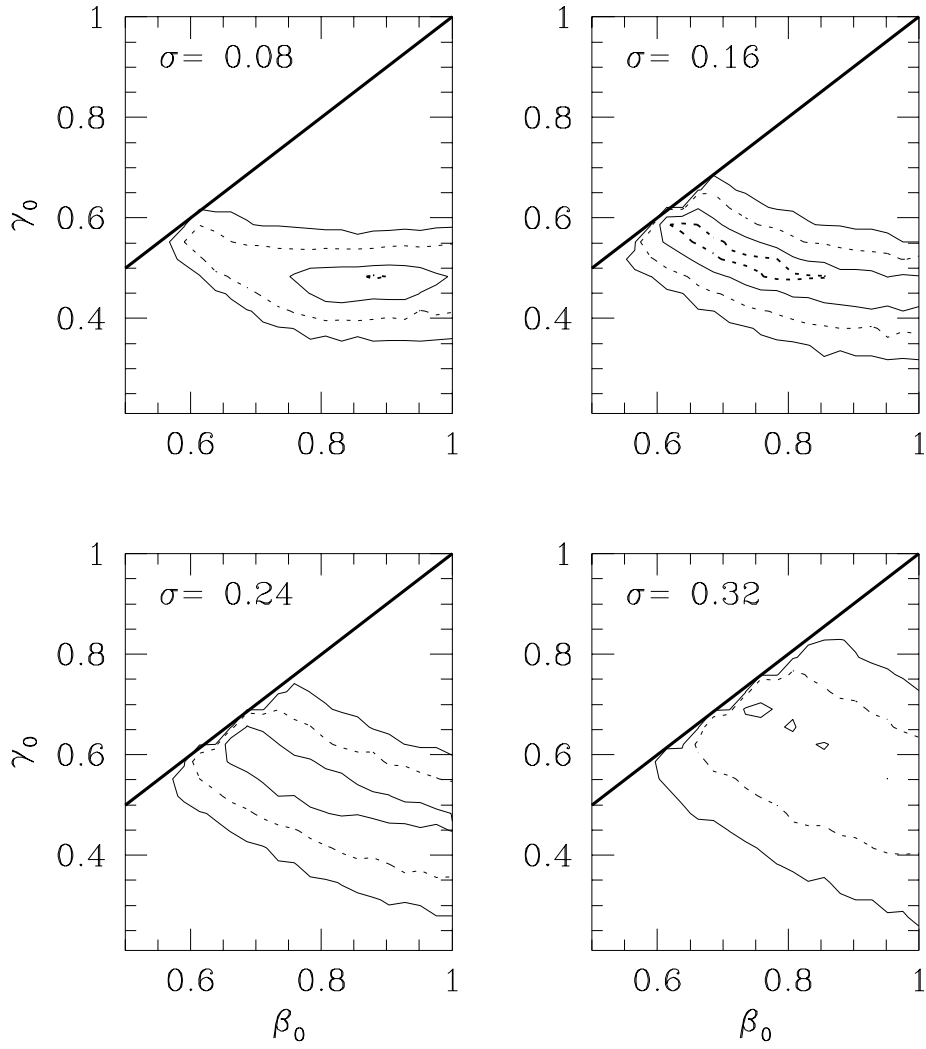


**Figure 6a:** Isoprobability contours, as measured by KS tests, on 4 slices through  $(\beta_0, \gamma_0, \sigma)$  parameter space. The fits are for the 62 galaxies in the BCD sample. Contours are drawn at the levels  $P_{KS} = 0.01, 0.1, 0.5,$  and  $0.9$  from outside.

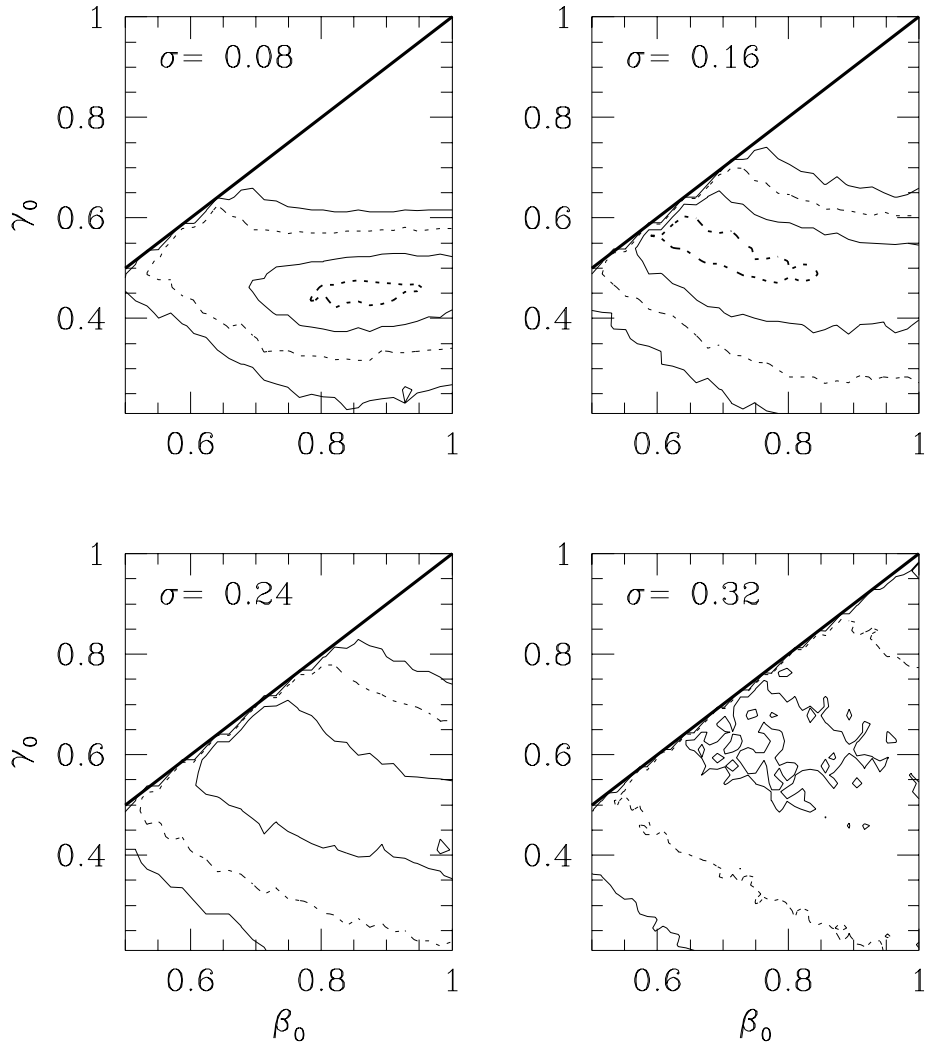


**Figure 6b:** Isoprobability contours, as measured by  $\chi^2$  tests, on 4 slices through  $(\beta_0, \gamma_0, \sigma)$  parameter space. The fits are for the 62 galaxies in the BCD sample. Contours are drawn at the levels  $P_{\chi^2} = 0.01, 0.1, 0.5,$  and  $0.9$  from outside.

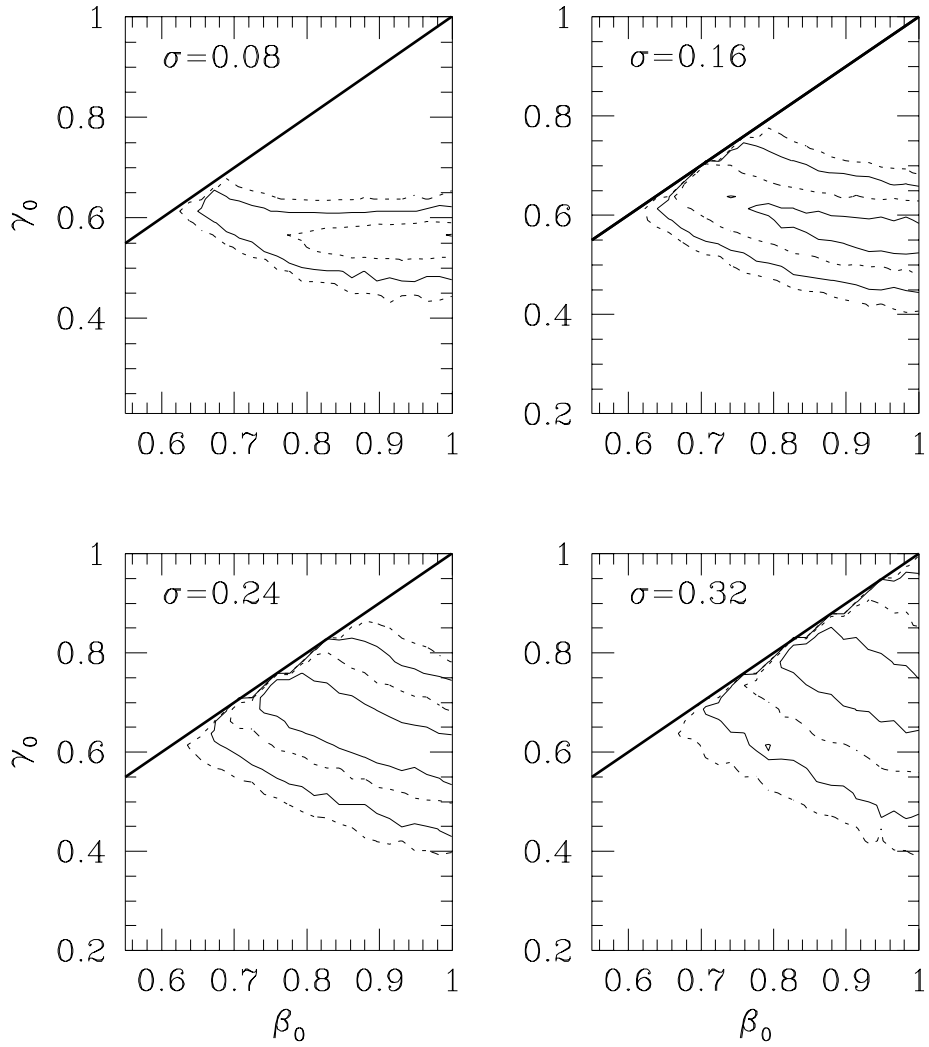


**Figure 7:** Isoprobability contours, as measured by KS tests, on 4 slices through  $(\beta_0, \gamma_0, \sigma)$  parameter space. The fits are for the 80 galaxies in the dE sample. Contours are drawn at the levels  $P_{\text{KS}} = 0.01, 0.1, 0.5,$  and  $0.9$ .